Available online at www.sciencedirect.com
SCIENCE DIRECT®
International Journal of Heat and Fluid Flow 26 (2005) 474–484
International Journal of HEAT AND FLUID FLOW
www.elsevier.com/locate/ijhff

A hydrodynamic CHF model for downward facing boiling on a coated vessel

J. Yang, F.B. Cheung *

Department of Mechanical and Nuclear Engineering, The Pennsylvania State University, 215 Reber Building, University Park, PA 16802-1412, USA

Received 6 June 2004; accepted 30 September 2004

Abstract

A hydrodynamic critical heat flux (CHF) model has been developed in this study for downward facing boiling on the outer surface of a hemispherical vessel with micro-porous layer coatings. The CHF model considers the vapor dynamics and the boiling-induced two-phase motions in three separate regions adjacent to the heating surface. These include a micro-porous coating layer, a liquid sublayer, and a two-phase boundary layer. Mathematical formulation of the CHF model has been made, taking into account the flow paths to an evaporation site within the porous coating layer, the behavior of the liquid sublayer, and the fluid motions of the two-phase boundary layer. It is found that the local CHF limit is reached when the liquid supply from the two-phase boundary layer through the liquid sublayer and the micro-porous coating to the heating surface is not sufficient to prevent local dryout of the heating surface. The dryout process consists of two sequential stages. In the initial stage, the vapor slug that forms by the downward facing boiling process moves toward the micro-porous coating layer owing to the depletion of the liquid sublayer. In the final stage, depletion of the capillary-assisted liquid supply occurs in the micro-porous coating layer, resulting in the dryout of the heating surface. This is followed by an abrupt increase in the local surface temperature, marking the occurrence of CHF. Comparison of the hydrodynamic CHF model with experimental data has been made and the results are found to be quite satisfactory.

Keywords: Critical heat flux; Micro-porous layer coating; Downward facing boiling; Two-phase flow

1. Introduction

To improve the ability of high-level decay heat removal during external passive cooling of the lower head of a nuclear reactor vessel, it has been proposed that surface coating be used to facilitate the process of downward facing boiling on the vessel outer surface. Water is made available on the bottom side of the reactor vessel by flooding the reactor cavity during a severe core-meltdown accident. By applying a suitable surface coating on the external surface of the lower head, enhanced boiling of water in the flooded cavity can be obtained. One surface coating being considered is the class of micro-porous layer coatings. Micro-porous layer coatings are extra-thin porous-layer coatings having layer thicknesses that are less than the superheated liquid layer thickness for activation of the cavities during nucleation (Chang and You, 1997). The use of a thin surface coating has been experimentally shown to be an effective passive enhancement technique by many researchers. O'Connor and You (1995) found a 109% increase in the CHF limit over a non-painted surface in saturated FC-72 with almost an 80% reduction in nucleate boiling superheat. Chang and You (1996) obtained approximately an 80% reduction in incipient superheat, 330% enhancement in nucleate boiling heat transfer, and

* Corresponding author. Tel.: +1 814 863 4261; fax: +1 814 863 8682.
E-mail address: fxc4@psu.edu (F.B. Cheung).

0142-727X/$ - see front matter © 2004 Elsevier Inc. All rights reserved.
doi:10.1016/j.ijheatfluidflow.2004.09.003

Nomenclature

Capital letters

A_m	net flow area across liquid sublayer
A_p	flow cross-sectional area of porous medium
A_v	surface area occupied by all vapor jets
A_w	total heating surface underneath the porous layer coating
C_1	universal constant, Eq. (14)
C_2	universal constant, Eq. (16)
C_3	universal constant, Eq. (17)
C_4	universal constant, Eq. (21)
C_E	Ergun coefficient
C_f	friction coefficient
C_J	Leverett function constant number
$J(s)$	Leverett function
K	media permeability
L_b	dimensionless quantity for radius of the vessel
P_{max}	maximum pressure drop
P_c	capillary pressure
P_g	pressure inside the gas phase
p_l	pressure inside the liquid phase
Q''_{CHF}	dimensionless quantity for Critical Heat Flux
R	radius of vessel
R_c	radius of curvature of interface
U_g	dimensionless vapor velocity
U_l	dimensionless liquid velocity

Lower case letters

d	diameter of spherical metallic particle
g	gravitational force coefficient
h_{fg}	latent heat of vaporization
j_l	liquid velocity entrained from the ambient liquid
l	characteristic length of vapor slug
l_m	characteristic length of porous medium
m_p	rate of liquid supply from porous-layer coating
q''_{NB}	local nucleate boiling heat transfer rate
q''_{CHF}	local critical heat flux
q''_{CHF_0}	critical heat flux at initial location
t_v	vapor ejection cycle
$u_{l,p}$	liquid velocity within porous-layer coating
u_g	local vapor velocity
u_l	local liquid velocity
u_{g_0}	vapor velocity leaving initial location
u_{l_0}	liquid leaving initial location
v_g	local vapor jet velocity
v_l	local liquid jet velocity

Greeks

α	void fraction
δ	two-phase boundary layer thickness
δ_0	two-phase boundary layer thickness in the bottom center region
δ_m	liquid sublayer thickness
δ_p	thickness of porous-layer coating
ε	porosity of coating
θ	angular location
θ_0	angular position of initial location
μ	dynamic viscosity
ρ_l	liquid density
ρ_v	vapor density
σ	surface tension coefficient
τ_w	wall shear stress
τ_i	interfacial shear stress

Other letters

Ω	angle of inclination
Δ	dimensionless two-phase boundary thickness

Subscripts

c	capillary
l	liquid
g	gas
p	porous layer
CHF	critical heat flux

100% enhancement in CHF using micro-porous layer coatings made of copper particles (1–50 μm) and aluminum particles (1–20 μm). Dizon et al. (2003) obtained more than a 100% increase in the CHF value at different angular locations of a downward facing curved surface under transient quenching conditions. Liter and Kaviany (2001) reported an enhancement in CHF of nearly a factor of three using modulated porous-layer coatings.

Theoretically, a number of studies have been performed to investigate the CHF mechanisms for pool boiling on a plain surface. Carey (1992) reviewed four postulated mechanisms as the cause for the CHF phenomenon in pool boiling. Kutateladze (1948) first established a relation for CHF using dimensional analysis by linking the phenomenon of flooding to the CHF condition:

$$q''_{CHF} = C_k \rho_v^{1/2} h_{fg} [g(\rho_l - \rho_v)\sigma]^{1/4} \quad (1)$$

Zuber (1959) included Taylor wave motion and Helmhotz instability analysis in his CHF model. The model was further refined by Lienhard and Dhir (1973) as follows:

$$q''_{CHF} = C \rho_v h_{fg} \left[\frac{g(\rho_l - \rho_v)\sigma}{\rho_v^2} \right]^{1/4} \quad (2)$$

In Zuber's original model the constant on the right side of the above expression is $\pi/24$ while in the model proposed by Lienhard and Dhir the constant is equal to $\pi/[16(3)^{1/4}]$.

A number of phenomenological theories have been put forth to explain the CHF enhancement by using porous-layer coatings. The observed enhancement with porous-layer coating is attributed to several effects: capillary pumping action on the liquid supply flow, increased number of nucleation sites, extended heat transfer surface area and the availability of the vapor escape paths from the porous coating adjacent to the liquid pool. Although several models are available to predict the CHF value for upward-facing surfaces, virtually no theoretical studies have been completed for CHF enhancement on downward facing surfaces with porous-layer coatings. In all CHF models for an upward-facing surface the liquid path is proposed as vertical columns or stacks from the porous-layer coating to the vapor film, leading to two independent liquid choking mechanisms. One is based on Zuber hydrodynamic theory and the other one is based on the viscous drag surpassing the available capillary pumping within the porous layer (Liter and Kaviany, 2001). However, the above models can not be applied to the present work, as the liquid path is different due to the orientation of the downward facing surface. The rate of liquid supply is determined not only by the portion from the upward two-phase boundary layer flow but also by the capillary pumping flow within the porous media along the curved surface to the evaporation site. In another words, the limit of CHF would not be reached unless the sum of these two liquid supply mechanisms is not sufficient to maintain nucleate boiling under certain heating conditions.

In this study, a hydrodynamic CHF model is developed for downward facing boiling on a hemispherical vessel with a micro-porous coating layer, taking full account of the capillary effect of the vessel coating. Spatial variation of the local CHF limit on the vessel outer surface predicted by the model is compared with the experimental data recently obtained by Dizon et al. (2003) and Yang et al. (2004).

2. Theoretical modeling

As described in Fig. 1, there are three layers of interest. These include the thin surface coating sublayer, a liquid sublayer and a buoyancy-driven two-phase boundary layer. The surface coating sublayer refers to the micro-porous layer adjacent to the heating surface with liquid artery and vapor generation sites. The liquid sublayer corresponds to the layer underneath an elongated vapor slug growing over the surface coating. This liquid sublayer consists of a continuous liquid film with numerous micro-vapor jets. The buoyancy-driven two-phase boundary layer corresponds to the external buoyancy-driven two-phase boundary layer flow region. A detailed analysis of the flow and heat transfer for each layer is given below.

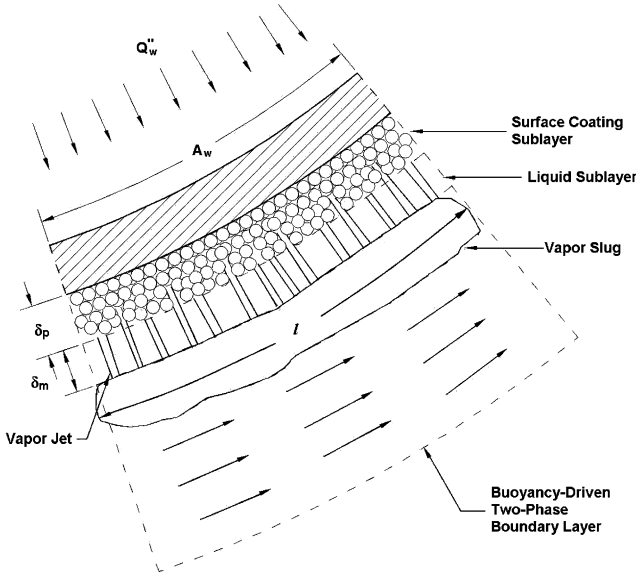

Fig. 1. Schematic of the sublayers underneath an elongated vapor slug.

2.1. Behavior of the porous-layer coating

The flow paths to an evaporation site within the porous-layer coating are critical to the occurrence of the CHF. Accurate description of the flow paths is not possible at this time, as the extremely complex liquid–vapor flow during downward facing boiling within the porous-layer coating is not well understood. The difficulty of visually observing the phenomenon within the thin coating hinders the understanding of the phenomenon. In this work, some simplifying assumptions are made regarding the flow paths in order to make the study of the CHF possible. First, it is assumed that there is complete phase separation within the coating where the vapor escapes from the void formed among the metal particles (see SEM photo in Fig. 2).

Second, when the local void shown in Fig. 2 is taken as the local representative elementary volume, this smallest differential volume will result in statistically meaningful local average properties. Adding extra pores (extra volume) around the representative elementary volume will not change the values of the local volume-averaged properties such as temperature and liquid velocity.

The liquid flow is idealized as entering toward the bottom of the porous layer, and then flowing along the surface matrix to the vapor generation zone. The vapor pressure is assumed to be constant at the saturation pressure everywhere in the system. As the process of

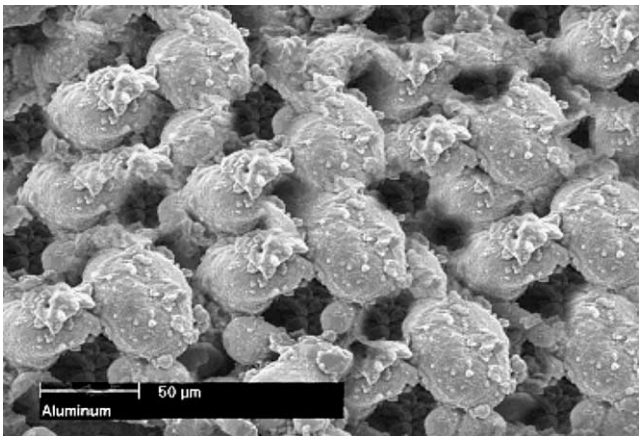

Fig. 2. SEM photos of an aluminum micro-porous layer coating.

depletion of capillary-assisted liquid supply approaches the critical condition, some deviations from the Darcy law are assumed. These deviations are due to the inertial contribution to the momentum balance. At any liquid supply velocity, the sum of the body force contribution, viscous contribution and inertial contribution make up the momentum balance for the flow. To account for the inertia effect, the pressure drop in the liquid through the porous coating is considered being governed by the Darcy–Ergun momentum relation (Kaviany, 1999):

$$\Delta p_{\mathrm{l}} = \rho_{\mathrm{l}} g \sin \Omega - \frac{\mu_{\mathrm{l}}}{K}\langle u_{\mathrm{l,p}}\rangle - \frac{C_{\mathrm{E}}}{K^{1/2}}\rho_{\mathrm{l}} \mid \langle u_{\mathrm{l,p}}\rangle \mid \langle u_{\mathrm{l,p}}\rangle \tag{3}$$

where $\langle u_{\mathrm{l,p}}\rangle$ is the magnitude of the volume-averaged liquid velocity vector through the liquid saturated region within the micro-porous coating layer. The $\langle u_{\mathrm{l,p}}\rangle$ describes the liquid supply motion toward the vaporization sites driven by local capillary-induced pressure gradient. K is the media permeability, C_{E} stands for the Ergun coefficient, and $K^{1/2}$ is used as the length scale. The quantity Ω indicates the angular location measured from the bottom center of the curved heating surface. The coefficient C_{E} represents deviation from the Stokes flow and the flow direction effect. Here the scalar form of C_{E} is used assuming that the angle between the direction of the pressure gradient of interest and the flow direction is zero. The Carmen–Kozeny model is used for the permeability, which predicts the value of K for packed beds reasonably well. This gives

$$K = \frac{\varepsilon^3 d^2}{180(1-\varepsilon)^2} \tag{4}$$

$$C_{\mathrm{E}} = \left(\frac{0.018}{\varepsilon^3}\right)^{1/2} \tag{5}$$

The porosity of the coating ε is assumed to be independent of the presence of a pressure gradient for the rigid surface coating matrices of interest. Although there are some porosity measurement techniques available, in this study photography is chosen because the length scale in the tangent direction of the matrix is much larger than the scale in the radial direction. By comparing the sum of areas of solid to the sum of areas of void, the porosity of the coating ε can be determined. The metallic particle diameter d is equal to 50 μm in this study, as shown in Fig. 2, and the coating porosity is about 0.4.

The coexistence of liquid and vapor within the voids of the micro-porous coating gives rise to capillary forces. As interfacial tension exists on the boundary between two phases in a pore space, the interface is curved and there is a capillary pressure difference across the interface. There is a maximum sustainable pressure drop across the characteristic length of the coating, which is assumed to be equal to the capillary pressure, i.e.,

$$p_{\max} = p_{\mathrm{g}} - p_{\mathrm{l}} = \frac{2\sigma}{R_{\mathrm{c}}} \tag{6}$$

where σ is the surface tension and R_{c} the radius of curvature of the interface.

Luikov (1966) derived an expression for the largest minimum pore diameter R_{c} of a system consisting of uniform spherical particles of small radius. With cubic packing, the largest minimum pore diameter has been determined as

$$R_{\mathrm{c}} = 0.41\frac{d}{2} \tag{7}$$

For a porous medium made of spherical metallic particles of $d = 50\,\mu\mathrm{m}$, this will give:

$$p_{\mathrm{c}} = \frac{4\sigma}{0.41d} = 11.473\ \mathrm{kPa} \tag{8}$$

Leverett (1976) defined a reduced capillary pressure function, which was subsequently named the Leverett J-function and used for relating the liquid saturation, media porosity and media permeability to the capillary pressure through the equation

$$p_{\mathrm{c}} = J(s)\frac{\sigma}{(K/\varepsilon)^{1/2}} \tag{9}$$

In the above relation, $J(s)$ is the Leverett function. For the maximum capillary pressure, the Leverett function is represented by a constant number C_J. According to Liter and Kaviany (2001), Scheidegger (1960) determined the value of $C_J = 0.523$ from the data presented by Leverett. Udell reported a value of 0.56 (1985). By utilizing the results of Luikov (1966) shown in Eq. (8), C_J would be 0.48 for the particle size of 50 μm which is in good agreement with the available data. In the subsequent analysis, the following equation is used to calculate the capillary pressure.

$$p_{\mathrm{c}} = C_J\frac{\sigma}{(K/\varepsilon)^{1/2}} \tag{10}$$

The maximum liquid velocity within the porous media is obtained through the momentum balance given by Eq.

(3) along with the available capillary force given by Eq. (10). The liquid supply velocity below the critical condition within the porous media can be linearly related as a fraction of this maximum velocity, where the ratio is determined by the media geometric parameters. Inserting Eq. (10) into Eq. (3) one can explicitly solve for $\langle u_{l,p}\rangle$:

$$-\frac{C_J\sigma}{(K/\varepsilon)^{1/2}l_m}=-\frac{\mu_l}{K}\langle u_{l,p}\rangle-\frac{C_E}{K^{1/2}}\rho_l\langle u_{l,p}\rangle^2$$

$$\langle u_{l,p}\rangle=\frac{K^{1/2}}{2C_E\rho_l}\left[\left(\frac{\mu_l^2}{K^2}+\frac{4C_E\rho_lC_J\sigma}{K^{1/2}(K/\varepsilon)^{1/2}l_m}\right)^{1/2}-\frac{\mu_l}{K}\right] \tag{11}$$

where length l_m represents the length for the porous medium. The characteristic length l_m represents the length that the liquid flow needs to go through toward the vaporization sites. In deriving Eq. (11), the effect of gravity is assumed to be negligible since the capillary effect dominates in the micro-porous coating layer. In terms of the characteristic length, l, of the vapor slug (see Fig. 1), the net flow cross-sectional area A_p can be expressed by

$$A_p\sim\varepsilon\delta_p l \tag{12}$$

where δ_p is the thickness of the micro-porous layer coating.

It follows that the local rate of liquid supply, m_p, from the micro-porous layer coating to the heating surface is given by

$$\dot{m}_p=\rho_l A_p\langle u_{l,p}\rangle \tag{13}$$

2.2. Behavior of the liquid sublayer

Cheung and Haddad (1997) combined the Helmholtz wavelength analysis (Carey, 1992) with Haramura and Katto's statement (1983) that the micro-layer area ratio is a function of the density ratio, to relate the liquid sublayer thickness, δ_m, to the relative velocity between the vapor jets and the liquid:

$$\delta_m=C_l\lambda_H=\frac{2C_1\pi\sigma}{\rho_g}\left(1+\frac{\rho_g}{\rho_l}\right)|\langle v_g\rangle-\langle v_l\rangle|^{-2} \tag{14}$$

and

$$\frac{\langle v_g\rangle}{\langle v_l\rangle}=\frac{\rho_l}{\rho_g}\left(\frac{A_w}{A_v}-1\right) \tag{15}$$

where A_v is the surface area occupied by all the vapor jets, and A_w is the total heating surface area underneath the micro-porous layer coating. The quantities $\langle v_g\rangle$ and $\langle v_l\rangle$ represent the local vapor jet and liquid velocities, respectively. According to the finding of Haramura and Katto (1983), we have:

$$\frac{A_v}{A_w}=C_2\left(\frac{\rho_g}{\rho_l}\right)^{1/5} \tag{16}$$

Combination of Eqs. (14)–(16) gives:

$$\delta_m=C_3\sigma\rho_g\left(1+\frac{\rho_g}{\rho_l}\right)\left(\frac{\rho_g}{\rho_l}\right)^{0.4}\left(\frac{h_{fg}}{q''_{NB}}\right)^2 \tag{17}$$

The net flow area across the liquid sublayer can be expressed by

$$A_m\sim\delta_m l \tag{18}$$

Thus the local rate of liquid supply, m_s, from the two-phase boundary layer to the liquid sublayer is given by

$$\dot{m}_s=\rho_l\langle u_l\rangle A_m \tag{19}$$

2.3. Occurrence of the local CHF

The local critical heat flux limit is reached when the liquid supply from the two-phase boundary layer through the liquid sublayer and the micro-porous coating to the heating surface is not sufficient to prevent local dryout. This process comprises two steps. In the first step, the vapor slug moves toward the surface-coating sublayer as a result of the depletion of the liquid sublayer. In the second step, depletion of the capillary-assisted liquid supply in the micro-porous coating initiates the local dryout process. This marks the occurrence of the local CHF that leads to an abrupt increase in the local temperature of the heating surface. From Eqs. (13) and (19), an expression for the local critical heat flux can be obtained, based on a local energy balance, by setting the sum of m_p and m_s equal to the rate of the liquid depletion at the local CHF:

$$\frac{q''_{CHF}A_w}{h_{fg}}=\rho_l\langle u_l\rangle\delta_m l+\rho_l\frac{K^{1/2}}{2C_E\rho_l}\left[\left(\frac{\mu_l^2}{K^2}+\frac{4C_E\rho_lC_J\sigma}{K^{1/2}(K/\varepsilon)^{1/2}l_m}\right)^{1/2}-\frac{\mu_l}{K}\right]\varepsilon\delta_p l \tag{20}$$

From the two-phase boundary layer flow observations by Cheung and Haddad (1994, 1995), the characteristic length l, is found to be proportional to the local two-phase boundary layer thickness, δ_0, in the bottom center region, i.e.

$$l=C_4\delta_0 \tag{21}$$

where C_4 is an empirical constant having a value very close to four along the curved heating surface. As discussed by Cheung and Haddad (1994, 1995), the CHF point is a continuation of the nucleate boiling regime in the high heat flux region. Helmholtz instability is acting upon the micro-vapor jets throughout the entire high heat flux nucleate boiling regime including the CHF point. Hence, Eq. (17) should be applicable to the CHF limit. By setting q''_{NB} equal to q''_{CHF} in Eq. (20), the following equation is obtained for the occurrence of CHF:

$$A(q''_{\mathrm{CHF}})^3 - B(q''_{\mathrm{CHF}})^2 - C = 0 \tag{22}$$

where the coefficients are given by

$$A = \frac{A_{\mathrm{w}}}{h_{\mathrm{fg}}} \tag{23}$$

$$B = \frac{K^{1/2}}{2C_{\mathrm{E}}}\left[\left(\frac{\mu_{\mathrm{l}}^2}{K^2} + \frac{4C_{\mathrm{E}}\rho_{\mathrm{l}}C_J\sigma}{K^{1/2}(K/\varepsilon)^{1/2}l_{\mathrm{m}}}\right)^{1/2} - \frac{\mu_{\mathrm{l}}}{K}\right]\varepsilon\delta_{\mathrm{p}}C_4\delta_0 \tag{24}$$

$$C = \rho_{\mathrm{l}}\langle u_{\mathrm{l}}\rangle C_4 C_3 \delta_0 \sigma \rho_{\mathrm{g}} h_{\mathrm{fg}}^2 \left(1 + \frac{\rho_{\mathrm{g}}}{\rho_{\mathrm{l}}}\right)\left(\frac{\rho_{\mathrm{g}}}{\rho_{\mathrm{l}}}\right)^{0.4} \tag{25}$$

The quantity, $\langle u_{\mathrm{l}}\rangle$ in Eq. (25) can be determined from the following two-phase boundary layer flow analysis.

2.4. Behavior of the two-phase boundary layer

During the heating process, a large amount of vapor would be generated as a result of downward facing boiling of water on the heating surface. Under the influence of buoyancy, the vapor would flow upward along the curved outer surface of the vessel. The ambient liquid water, which is saturated and quiescent initially, would be entrained by the vapor flow, thus resulting in a buoyancy-driven upward co-current two-phase flow along the boundary layer.

It is not necessary to develop a comprehensive analytical model for the liquid–vapor two-phase flow as the main focus here is the local heat transfer enhancement by the micro-porous layer coating. A simplified system of governing equations (Carey, 1992) with the ability to provide an accurate assessment of the local quantity, $\langle u_{\mathrm{l}}\rangle$, in Eq. (25) is used in this study. Although information regarding the local behavior of the flow is lost in doing so, the model provides the required information for predicting the local CHF value. A schematic of the two-phase boundary layer is shown in Fig. 3.

The momentum for the vapor–liquid mixture in the two-phase boundary layer is governed by the following differential equation:

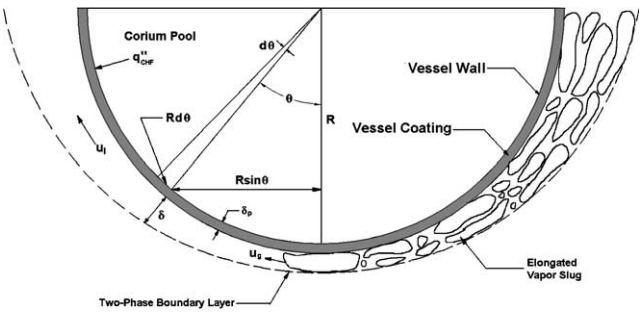

Fig. 3. Two-phase boundary layer on the outer surface of a hemispherical vessel coated with a micro-porous layer.

$$\frac{\mathrm{d}}{\mathrm{d}\theta}\{[\rho_{\mathrm{g}}\alpha u_{\mathrm{g}}^2 + \rho_{\mathrm{l}}(1-\alpha)u_{\mathrm{l}}^2]\delta\sin\theta\} = \alpha\delta Rg(\rho_{\mathrm{l}} - \rho_{\mathrm{g}})\sin^2\theta - (\tau_{\mathrm{w}} + \tau_{\mathrm{i}})R\sin\theta \tag{26}$$

where τ_{w} and τ_{i} represents the wall and the interfacial shear stresses. These quantities are given by Cheung and Epstein (1987):

$$\tau_{\mathrm{w}} + \tau_{\mathrm{i}} = 0.5C_{\mathrm{f}}[\alpha u_{\mathrm{g}} + (1-\alpha)u_{\mathrm{l}}][\rho_{\mathrm{g}}\alpha u_{\mathrm{g}} + \rho_{\mathrm{l}}(1-\alpha)u_{\mathrm{l}}] \tag{27}$$

where C_{f} is a friction coefficient having the value of 0.005.

The mass flow rate across the thickness of the two-phase boundary layer is governed by the following differential equation:

$$\frac{\mathrm{d}}{\mathrm{d}\theta}[(1-\alpha)u_{\mathrm{l}}\delta\sin\theta] = j_{\mathrm{l}}R\sin\theta \tag{28}$$

where j_{l} is the net liquid velocity entrained from the ambient fluid into the two-phase boundary layer at θ. In this case, j_{l} only represents the liquid mass swept into the boundary layer by the upward motion induced by vapor generation, excluding the portion of liquid mass depletion due to boiling on the heating surface. Similarly, the vapor mass across the thickness of the two-phase boundary layer under saturated boiling conditions at a given location θ is governed by the following equation:

$$\frac{\mathrm{d}}{\mathrm{d}\theta}[\alpha u_{\mathrm{g}}\delta\sin\theta] = \frac{q''_{\mathrm{CHF}}R\sin\theta}{\rho_{\mathrm{g}}h_{\mathrm{fg}}} \tag{29}$$

In Eq. (29), the heat flux is set equal to the local CHF value so that the local vapor and liquid velocities would correspond to those appearing in Eq. (25). Note that the local CHF condition gives rise to the maximum local vapor/liquid velocities and boundary layer thickness that can possibly be developed at a given downstream location.

It is necessary to have the relative velocity between the liquid and vapor phases to close the governing system. This is obtained by assuming that once the vapor mass departs from the heating surface, it would attain its terminal rise velocity relative to the liquid phase in the two-phase boundary layer (Wallis, 1969). Accordingly, the relative velocity is given by

$$u_{\mathrm{g}} = u_{\mathrm{l}} + 1.53\left[\frac{\sigma g\sin\theta(\rho_{\mathrm{l}} - \rho_{\mathrm{g}})}{\rho_{\mathrm{l}}^2}\right]^{1/4} \tag{30}$$

Eqs. (26)–(30) complete the governing system for the buoyancy-driven external two-phase boundary layer flow.

2.5. Initial conditions and the universal constants

To solve Eqs. (22)–(30) simultaneously for the spatial variation of the local CHF, it remains necessary to

determine the initial value of the two-phase boundary layer thickness at the bottom center of the vessel. To do so, the vapor mass that forms in the bottom center region needs to be considered. The initial location is chosen as the bottom center surface at a small θ_0 away from the vertical axis. Since $\theta_0 \ll \pi/2$, the local critical heat flux can be treated as a constant equal to $(q''_{\mathrm{CHF}})_0$. The vapor velocity leaving initial location, u_{g_0}, can be determined from a mass balance:

$$\rho_g u_{g_0} \alpha (2\pi R \delta_0 \sin\theta_0) = \frac{1}{h_{fg}} \int_0^{\theta_0} q''_{\mathrm{CHF}} 2\pi R^2 \sin\theta \, d\theta \tag{31}$$

This leads to

$$u_{g_0} = \frac{(q''_{\mathrm{CHF}})_0}{\alpha \rho_g h_{fg}} \left[\frac{1-\cos\theta_0}{\sin\theta_0}\right] \left(\frac{R}{\delta_0}\right) \tag{32}$$

From Eq. (30), it can be shown that

$$u_{l0} = u_{g_0} - 1.53 \left[\frac{\sigma g \sin\theta_0 (\rho_l - \rho_g)}{\rho_l^2}\right]^{1/4} \tag{33}$$

Based upon the vapor dynamics observed by Cheung and Haddad (1994, 1995), the aspect ratio of the vapor mass is very close to four, i.e., $C_4 = 4$ in Eq. (21). There is another universal constant, C_3, that needs to be determined from experimental data. To do this, the vapor dynamic and the local CHF limits at $\theta = \theta_0$ observed by Dizon et al. (2003) are employed. The occurrence of the local CHF limit in the bottom center region is the result of liquid depletion within the liquid sublayer and the micro-porous coating before the departure of the vapor mass from the heating surface. The mass of the liquid sublayer is $\rho_l \delta_m (A_w - A_v)$, whereas the mass of liquid hold up in the micro-porous coating under the same heating area is $\rho_l \delta_p \varepsilon A_w$. The total rate of the nucleate boiling heat transfer is q''_{NB}. The observed duration of the vapor ejection cycle is t_v, as such local dryout would occur if $q''_{\mathrm{NB}} A_w t_v / h_{fg}$ becomes equal to or larger than the mass of the total liquid available in the bottom center region. Thus, the local CHF limit at the bottom center is given by

$$(q''_{\mathrm{CHF}})_0 = \frac{h_{fg}}{t_v} \left[\rho_l \delta_m \left(1 - \frac{A_v}{A_w}\right) + \rho_l \delta_p \varepsilon\right] \tag{34}$$

where δ_m is given by Eq. (17). This leads to

$$C_3 = \left(\frac{(q''_{\mathrm{CHF}})_0 t_v}{h_{fg}} - \rho_l \delta_p \varepsilon\right) \Bigg/ \rho_l \sigma \rho_g \left(1 + \frac{\rho_g}{\rho_l}\right) \left(\frac{\rho_g}{\rho_l}\right)^{0.4} \left[\frac{h_{fg}}{(q''_{\mathrm{CHF}})_0}\right]^2 \tag{35}$$

where the term involving the area ratio has been ignored since $A_v/A_w \ll 1$.

According to the experimental observations reported by Dizon et al. (2003) and Cheung and Haddad (1994, 1995), the duration t_v was found to be 0.2 s whereas the local CHF limit was 0.85 MW/m^2. Using the properties for water at one atmosphere pressure, the value of C_3 is calculated to be 0.00141.

3. Numerical calculations

Eqs. (22)–(30) form a complete set of coupled equations governing the local variations of the CHF, q''_{CHF}, the vapor and liquid velocities u_g and u_l, respectively, the two-phase boundary layer thickness, δ, and the void fraction, α. The liquid entrainment rate, j_l in Eq. (28) is needed to solve this set of equations, however, no experimental data or relation on the liquid entrainment for such case is available to date. To circumvent this difficulty, the local void fraction in the two-phase boundary layer is postulated to be a constant value as the CHF limit is approached on the heating surface. This postulation has been justified by Cheung and Haddad (1997) based on their experimental observations (1994, 1995). According to the experimental data of Cheung and Haddad (1994, 1995), α is set equal to 0.915. Thus, Eq. (28), which contains the liquid entrainment term, can be eliminated from the governing system. The remaining unknown quantities (i.e. $q''_{\mathrm{CHF}}, u_g, u_l$ and δ) can be determined from Eqs. (22)–(27) and Eqs. (29) and (30) through numerical calculations.

To update the local value $q''_{\mathrm{CHF}}, u_g, u_l$ and δ, control volumes are assigned, distributed evenly, along the curved heating surface starting from the bottom center region to the hemisphere equator. With initial values of $q''_{\mathrm{CHF}}, u_g, u_l$ and δ, which are determined and discussed in the previous section, Eqs. (26) and (29) could be numerically integrated over the control volumes, however, the local CHF limit is updated through the following implicit relation derived from Eq. (23):

$$q''_{\mathrm{CHF}} = \sqrt{\frac{C}{A q''_{\mathrm{CHF}} - B}} \tag{36}$$

where A, B and C are given by Eqs. (23)–(25).

4. Results and discussion

Numerical calculations of the local boundary layer flow quantities, the local liquid supply velocity and the local CHF limits have been made for water along the curved porous-layer-coated heating surface. The vessel diameter has been treated as a parameter in these calculations. Results are shown in Figs. 4–9. To better show the physical size effect of the vessel, dimensionless quantities for the two-phase boundary thickness, vapor/liquid velocities and local CHF limit are defined in the following,

$$L_b = \frac{1}{R} \left[\frac{\sigma}{g(\rho_l - \rho_g)}\right]^{1/2} \tag{37}$$

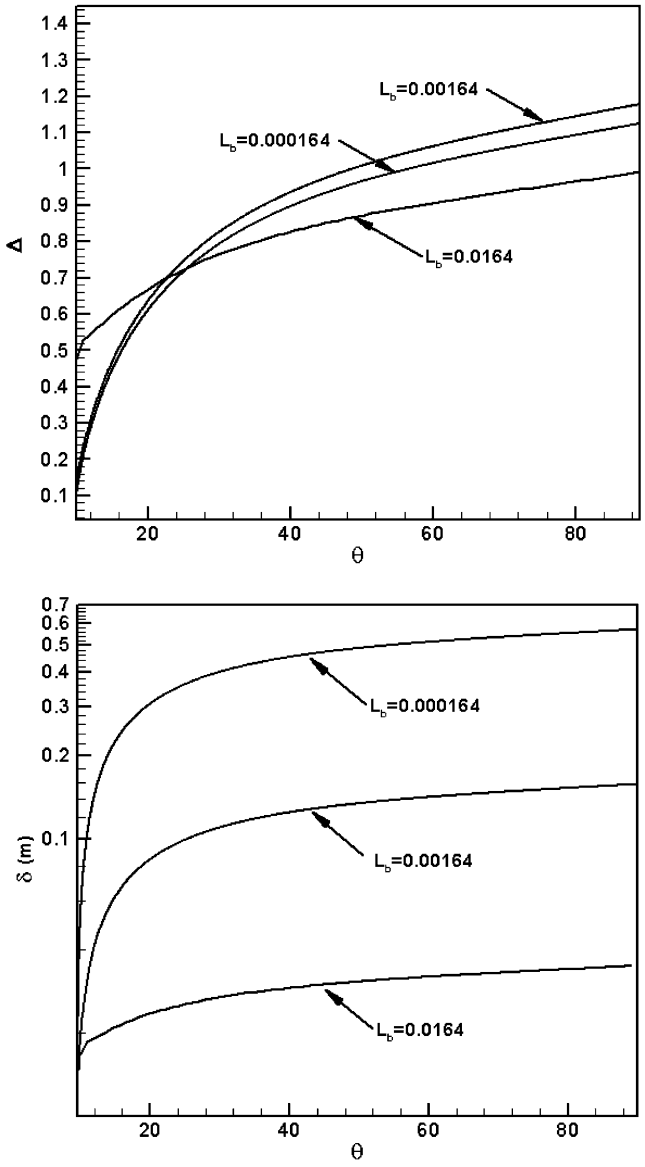

Fig. 4. Spatial variation of the local two-phase boundary layer thickness.

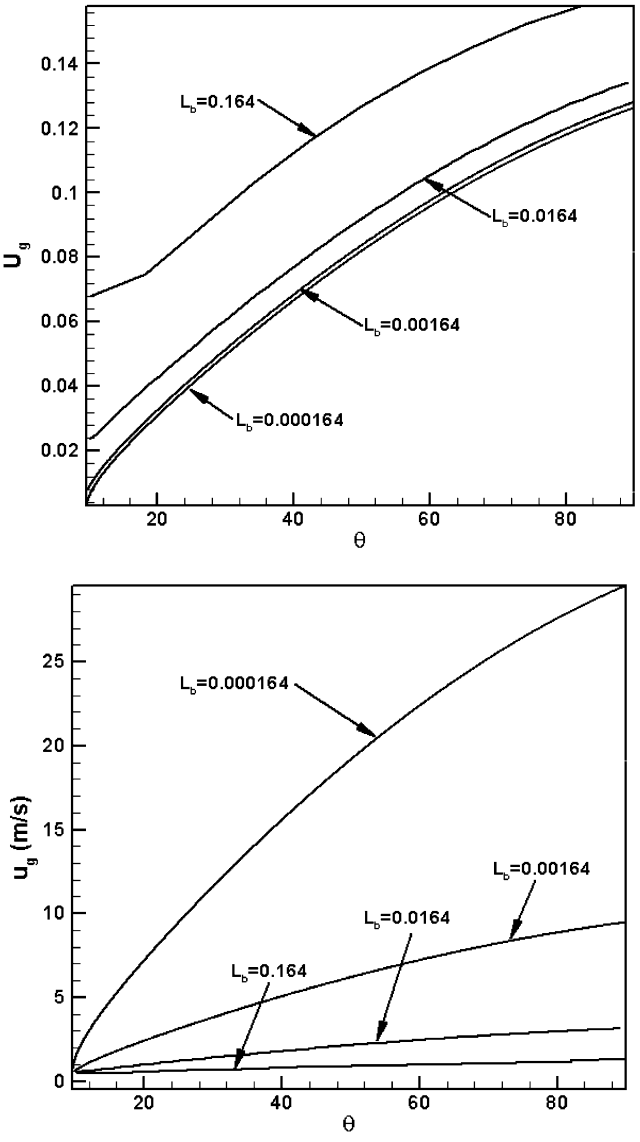

Fig. 5. Spatial variation of the local vapor velocity in the two-phase boundary layer.

$$Q_{\mathrm{CHF}} = \left[\frac{\rho_{\mathrm{g}}^2}{\sigma g(\rho_{\mathrm{l}}-\rho_{\mathrm{g}})}\right]^{1/4}\left(\frac{\rho_{\mathrm{l}}}{\rho_{\mathrm{l}}+\rho_{\mathrm{g}}}\right)^{1/3}\left(\frac{q''_{\mathrm{CHF}}}{\rho_{\mathrm{g}}h_{\mathrm{fg}}R^{0.059}}\right) \tag{38}$$

$$\Delta = \left[\frac{g(\rho_{\mathrm{l}}-\rho_{\mathrm{g}})}{\sigma}\right]^{1/4}\left(\frac{\rho_{\mathrm{g}}}{\rho_{\mathrm{l}}}\right)\left(\frac{\delta}{R^{0.578}}\right) \tag{39}$$

$$U_{\mathrm{g}} = \left[\frac{\rho_{\mathrm{g}}}{Rg(\rho_{\mathrm{l}}-\rho_{\mathrm{g}})}\right]^{1/2}\left(\frac{\rho_{\mathrm{g}}}{\rho_{\mathrm{l}}}\right)^{-0.1}u_{\mathrm{g}} \tag{40}$$

$$U_{\mathrm{l}} = \left[\frac{\rho_{\mathrm{l}}}{Rg(\rho_{\mathrm{l}}-\rho_{\mathrm{g}})}\right]^{1/2}u_{\mathrm{l}} \tag{41}$$

Physically, L_{b} represents the ratio between the characteristic bubble size and the radius of the vessel. For all values of L_{b}, the two-phase boundary layer thickness increases considerably from the bottom center to the upper edge of the vessel (see Fig. 4). It can be seen by comparing the dimensionless quantity to the actual value of the two-phase boundary layer thickness that the size effect becomes less important as the vessel diameter increases. For $L_{\mathrm{b}} = 0.000164$ ($D = 30.5\,\mathrm{m}$) and $L_{\mathrm{b}} = 0.00164$ ($D = 3.05\,\mathrm{m}$), the dimensionless two-phase boundary layer thicknesses are very close to one another. However, the actual thickness of the two-phase boundary layer is a strong function of L_{b} because the heating surface increases as the square of the vessel diameter.

The spatial variations of the vapor and liquid velocities are presented in Figs. 5 and 6, respectively. For all vessel sizes, the vapor and liquid velocities increase by

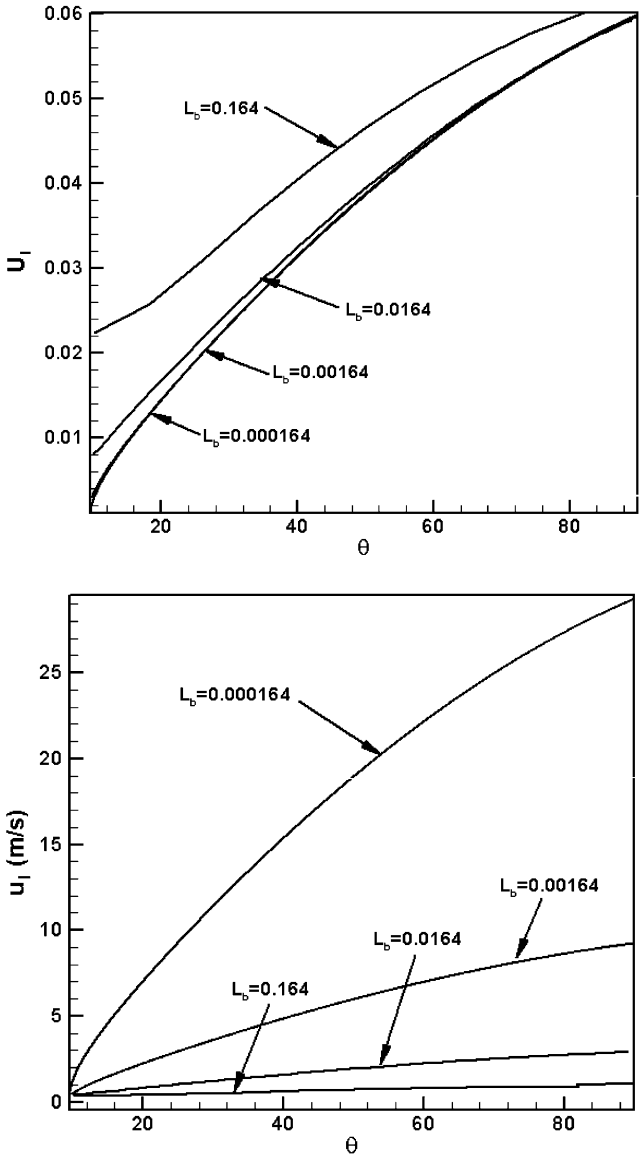

Fig. 6. Spatial variation of the local liquid velocity in the two-phase boundary layer.

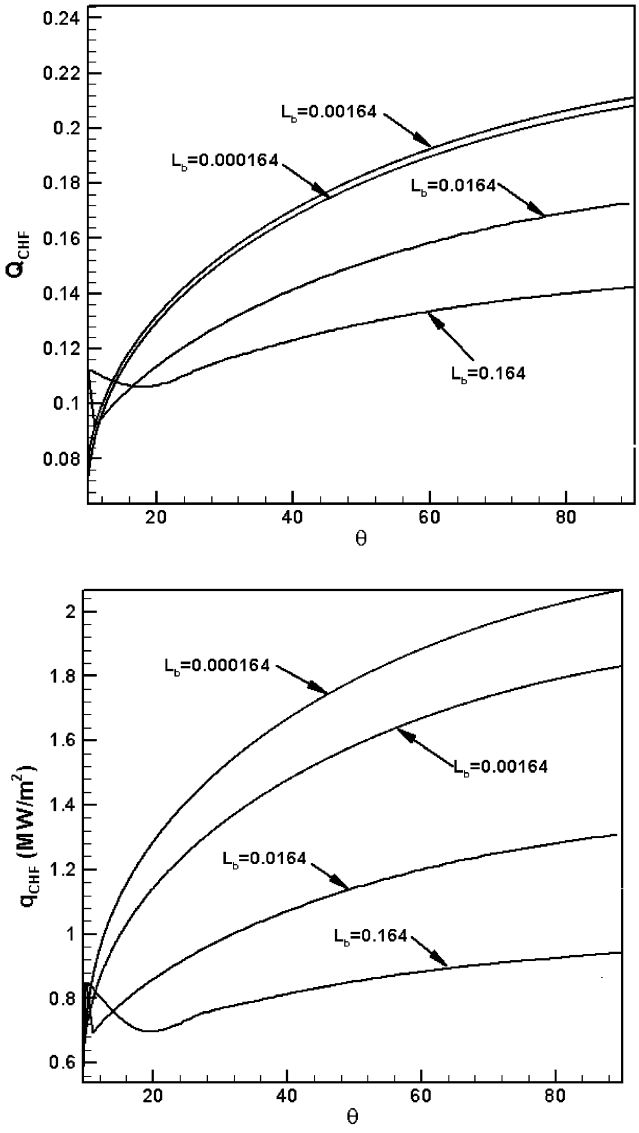

Fig. 7. Spatial variation of the local CHF on the coated heating surface.

more than an order of magnitude from the bottom center to the upper edge of the vessel. The relative velocity between the liquid and vapor phases is on the same order of the vapor and liquid velocities when θ is small. For large values of θ, the relative velocity is an order of magnitude smaller than the liquid and vapor velocities. The effect of L_b is quite strong on u_l and u_g, but very weak on the dimensionless quantities U_l and U_g. For vessels larger than 0.3 m ($L_b < 0.0164$), u_l and u_g would vary according to the square root of the vessel diameter whereas U_l and U_g are essentially independent of the vessel size.

Fig. 7 shows the spatial variation of the local critical heat flux predicted by the model. The dimensionless quantity Q_{CHF} appears to be a weak function of the vessel size especially when the vessel diameter becomes large. This clearly demonstrates the fact that for heated vessels with diameters considerably larger than the characteristic bubble size, the critical heat flux is weakly dependent of the vessel size. Note that away from the bottom center region the local critical heat flux increases from the bottom center to the upper edge of the vessel. This result is similar to the spatial variations of CHF observed experimentally by Dizon et al. (2003). As the local liquid velocity increases more than an order of magnitude along the vessel outer surface, there is a large increase in the local liquid supply rate, resulting in a significant increase in the local critical heat flux. Note, however, that there is a local peak value of CHF at the bottom center where the local liquid supply rate is higher due to the convergent effect. This result is consistent with the behavior observed experimentally by Dizon et al. (2003).

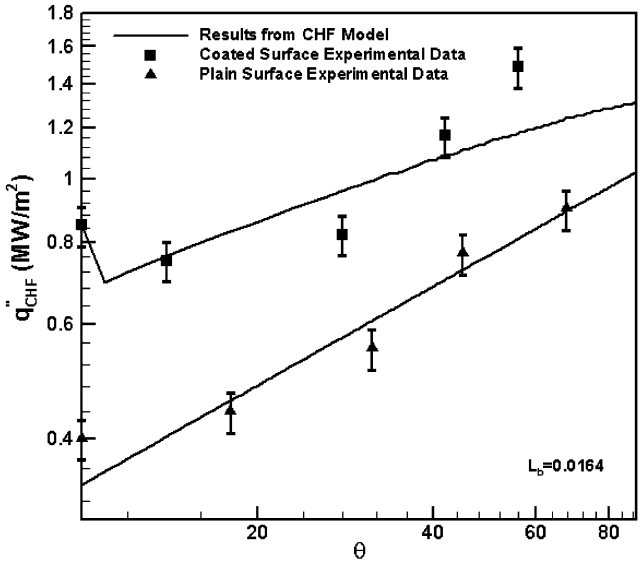

Fig. 8. Comparison of the predicted CHF with experimental data ($L_b = 0.0164$).

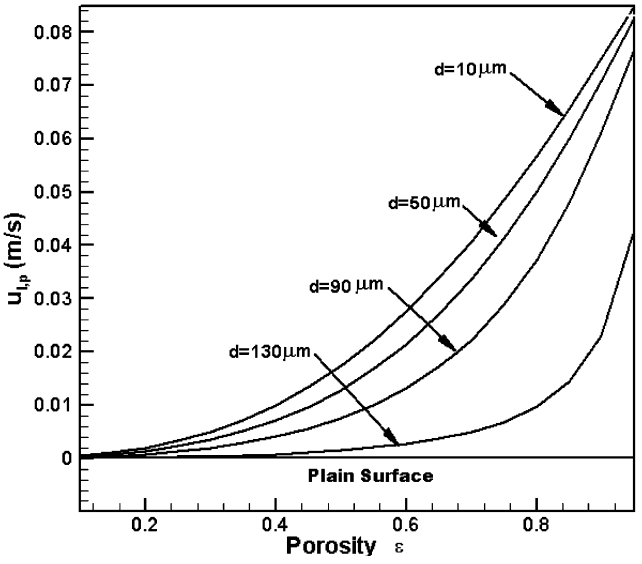

Fig. 9. Liquid supply velocity through the micro-porous layer coating.

Fig. 8 shows the predicted local critical heat flux together with the experimental data from Dizon et al. (2003) and Cheung and Haddad (1994, 1995). For the same vessel size $L_b = 0.0164$ ($D = 0.305$ m), the predicted CHF limits agree reasonably well with the experimental data. It should be noted that in the work of Dizon et al. (2003), uncertainties in the data acquisition system and the thermocouple resistance could cause slight fluctuations in the CHF value recorded. Thus, the experimental data do not display a smooth profile compared to the predicted CHF limits. Note that for a plain surface, the CHF limit increases monotonically with θ, which is different than the trend showed for the coated surface. For a coated vessel, the present model predicts a local peak at the bottom center with the local CHF limit decreasing in the downstream locations for small values of θ. This predicted behavior is consistent with that observed by Dizon et al. (2003). This behavior is due to the convergent effect on the local liquid supply at the bottom center, where the liquid could enter from all radial directions through the porous layer coating such that it helps prevent dryout at the bottom center, thereby increasing the local CHF limit. Another possible physical explanation for such behavior could be due to the availability of vapor escape paths provided by the porous layer coating. According to the experimental observation, for a coated vessel, the vapor bubbles generated in the bottom center region did not tend to agglomerate and were smaller than those vapor slugs generated for a plain vessel that would cover the whole bottom center region. Such dispersed vapor bubbles in the bottom center region would help the escape of newly generated vapor bubbles such that the CHF limit in the bottom center region becomes larger than those in the immediate downstream locations.

By comparing the CHF limits for a plain surface reported by Cheung and Haddad (1994, 1995), the CHF enhancement effect of the micro-porous layer coating can be clearly seen. This enhancement is mainly attributed to several effects: capillary pumping action on the liquid supply flow, increased number of nucleation sites, extended heat transfer surface area and the availability of the vapor escape paths from the porous coating layer adjacent to the liquid pool. Among the four enhancement mechanisms, the capillary pumping action on the liquid supply through the porous layer is the dominant factor. The capillary induced liquid supply velocity is presented in Fig. 9. Although the magnitude of liquid supply velocity through the porous layer coating is much less than the liquid velocity of the two-phase boundary layer, such liquid supply to the vaporization sites on the heating surface prevents local dryout and enhances the local CHF limits. Note that the liquid supply rate from the porous layer coating increases monotonically with the porosity ε, owing to the influence of ε on the availability of the flow channel inside the coating. However, the liquid supply rate tends to decreases as the diameter of the particles increases, as can be seen from Eqs. (6) and (10). Smaller particles give rise to a larger capillary pressure force.

5. Conclusions

A hydrodynamic CHF model has been developed for downward facing boiling on the outer surface of a porous-layer-coated hemispherical vessel. The model represents a first attempt to discern the enhancement effect of

vessel coating on the local CHF limits for downward facing boiling on the vessel outer surface. Based upon the results of this study, the following conclusions can be made:

1. Local dryout of the heating surface occurs when the local rate of liquid supply from the two-phase boundary layer through the liquid sublayer and the micro-porous coating becomes smaller than the rate of depletion of the liquid film by boiling. This critical condition determines the maximum local wall heat flux leading to dryout corresponding to the local CHF limit.
2. There is a considerable enhancement of the local CHF limits due to the vessel coating. This enhancement is mainly due to the capillary pumping effect on the liquid supply through the flow path formed inside the micro-porous layer coating. The present model, which accounts for the capillary effect on the CHF enhancement, agrees favorably with the available experimental data.
3. There is a local peak at the bottom center where the local CHF limit is higher than those values immediately downstream. This behavior, which is distinctly different from that observed for a plain surface, is due to the convergent effect on the liquid supply rate at the bottom center. Liquid could enter from all radial directions through the porous layer coating such that it helps prevent dryout at the bottom center, thereby increases the local CHF limit.
4. The effect of the vessel size is relatively weak on the dimensionless two-phase flow quantities and the dimensionless critical heat flux. For a coated vessel with a diameter considerably larger than the characteristic bubble size, the dimensionless liquid and vapor velocities are essentially independent of the vessel diameter whereas the dimensionless CHF limit is a weak function of the vessel diameter.

Acknowledgments

This work was performed under DOE contract number DE-AC07-99ID13727. The authors are grateful for the financial support by the U.S. Department of Energy and the Korean Ministry of Science and Technology as part of the K-INERI program. The authors wish to express their gratitude to Dr. J.L. Rempe of INEEL, Prof. K.Y. Suh of SNU, and Dr. S.B. Kim of KAERI for their valuable comments.

References

Carey, V.P., 1992. Liquid–Vapor phase-change Phenomena, Series in Chemical and Mechanical Engineering. Taylor & Francis.

Chang, J.Y., You, S.M., 1997. Boiling heat transfer phenomena from micro-porous and porous surfaces in saturated FC-72. Int. J. Heat Mass Transfer 40 (18), 4437–4447.

Chang, J.Y., You, S.M., 1996. Heater orientation effects on pool boiling of micro-porous-enhanced surfaces in saturated FC-72. ASME J. Heat Transfer 118 (4), 937–943.

Cheung, F.B., Epstein, M., 1987. Two-phase gas bubble-liquid boundary layer flow along vertical and inclined surfaces. Nucl. Eng. Des. 99, 93–100.

Cheung, F.B., Haddad, K.H., 1994. Observation of the dynamic behavior of the two-phase boundary layers in the SBLB experiments. Proceedings of the Twenty-Second Water Reactor Safety Meeting, Vol. 2, Washington, DC, pp. 87–112.

Cheung, F.B., Haddad, K.H., 1995. Steady-state observations of critical heat flux phenomenon on a downward facing hemispherical surface. Proceedings of the Twenty Third Water Reactor Safety Meeting, Washington, DC.

Cheung, F.B., Haddad, K.H., 1997. A hydrodynamic critical heat flux model for saturated pool boiling on a downward facing curved heating surface. Int. J. Heat Mass Transfer 40 (6), 1291–1302.

Dizon, M.B., Yang, J., Cheung, F.B., 2003. Effects of surface coating on nucleate boiling heat transfer from a downward facing surface. ASME Summer Heat Transfer Conference.

Haramura, Y., Katto, Y., 1983. A new hydrodynamic model of critical heat flux, applicable widely to both pool and forced convection boiling on submerged bodies in satrurated liquids. Int. J. Heat Mass Transfer 26, 389–399.

Kaviany, M., 1999. Principles of Heat Transfer in Porous Media, second ed. Springer, New York.

Kutateladze, S.S., 1948. On the transition to film boiling under natural convection. Kotloturbostroenie 3, 10–15.

Leverett, M.C., 1976. Capillary behavior in porous solids. Trans. AIME 142, 152.

Lienhard, J.H., Dhir, V.K., 1973. Hydrodynamic predictions of peak pool-boiling heat fluxes from finite bodies. Trans. ASME, Ser. C, J. Heat Transfer 95, 152–158.

Liter, S.G., Kaviany, M., 2001. Pool-boiling CHF enhancement by modulated porous-layer coating: theory and ecperiment. Int. J. Heat Mass Transfer 44, 4287–4311.

Luikov, V., 1966. Heat and Mass Transfer in Capillary-porous Bodies. Pergamon.

O'Connor, J.P., You, S.M., 1995. A painting technique to enhance pool boiling heat transfer in FC-72. ASME J. Heat Transfer 117 (2), 387–393.

Scheidegger, E., 1960. The Physics of Flow through Porous Media. The Macmilian Company, New York.

Udell, K.S., 1985. Heat transfer in porous media considering phase change and capillary—the heat pipe effect. Int. J. Heat Mass Transfer 28 (2), 485–495.

Wallis, G.B., 1969. One-dimensional Two-Phase Flow. McGraw-Hill, New York.

Yang, J., Dizon, M.B., Cheung, F.B., Rempe, J.L., Suh, K.Y., Kim, S.B., 2004. Critical heat flux for downward facing boiling on a coated hemispherical surface, Proceedings HT-FED 2004, Paper HT-FED 2004-56056.

Zuber, N., 1959. Hydrodynamics aspects of boiling heat transfer. AEC report, AECU-4439.